High Energy Density Picoliter Zn-Air Batteries for Colloidal Robots and State Machines

Ge Zhang[1], Jing Fan Yang[1], David Gonzalez-Medrano[2], Marc Z. Miskin[2], Sungyun Yang[1], Volodymyr B. Koman[1], Yuwen Zeng[1], Sylvia Xin Li[1], Matthias Kuehne[1], Albert Tianxiang Liu[3], Allan M. Brooks[1], Mahesh Kumar[1,4] and Michael S. Strano[1]

[1]*Department of Chemical Engineering, Massachusetts Institute of Technology, Cambridge, MA 02139, USA.*

[2]*Department of Electrical and Systems Engineering, University of Pennsylvania, Philadelphia, PA 19104, USA.*

[3]*Physics Department, Stanford University, Palo Alto, CA 94305, USA.*

[4]*Department of Electrical Engineering, Indian Institute of Technology Jodhpur, 342030, India*

Correspondence author: Michael S. Strano, strano@mit.edu

Abstract

The recent interest in microscopic autonomous systems, including microrobots, colloidal state machines and smart dust has created a need for microscale energy storage and harvesting. However, macroscopic materials for energy storage have noted incompatibilities with micro-fabrication techniques, creating significant challenges to realizing microscale energy systems. Herein, we photolithographically pattern a microscale Zn/Pt/SU-8 system to generate the highest energy density microbattery at the picoliter (10^{-12} L) scale. The device scavenges ambient or solution dissolved oxygen for a Zn oxidation reaction, achieving an energy density ranging from 760 to 1070 Wh L^{-1} at scales below 100 μm lateral and 2 μm thickness in size. More than 10,000 devices per wafer can be released into solution as functional colloids with energy stored onboard. Within a volume of only 2 pL each, these primary microbatteries can deliver open circuit voltages of 1.05 ± 0.12 V with total energies ranging from 5.5 ± 0.3 to 7.7 ± 1.0 μJ and a maximum power near 2.7 nW. We demonstrate that such systems can reliably power a micron-sized memristor circuit, providing access to non-volatile memory. We also cycle power to drive the reversible bending of microscale bimorph actuators at 0.05 Hz for mechanical functions of colloidal robots. Additional capabilities such as powering two distinct nanosensor types and a clock circuit are also demonstrated. The high energy density, low volume and simple configuration promise the mass fabrication and adoption of such picoliter Zn-air batteries for micron-scale, colloidal robotics with autonomous functions.

Introduction

The past decade has witnessed a surge of interest in scaling down sensors, robots and computers to sub-millimeter regime. For example, researchers have managed to shrink the volume of smart dust by nearly 1,000 fold since its first proposal,[1,2] yet the volume is still on the order of microliters (mm^3).[3,4] More recently, novel materials and fabrication techniques have enabled even smaller sensors and machines invisible to naked eyes,[5-10] with their lateral dimensions smaller than 100 μm and their volume entering the *picoliter* (10^{-6} mm^3) regime. Such devices have been aerosolized,[8] embedded into a polymer matrix,[6] and injected into tissues.[6] A notable recent achievement consists of picoliter robots that can walk using bimorph actuators as legs.[7] However, energy storage has emerged as a limitation at the micron-scale, which creates challenges in both material selection and fabrication.[11] Conventional battery materials are prepared using wet chemistry that is fundamentally incompatible with the microelectronic fabrication processes used for these micro-robotic advances,[12] hence restricting most microbatteries to millimeters in size in the literature.[13-16] Sub-square-millimeter batteries were only reported very recently, but they were neither picoliter-sized nor colloidal.[17-19] In this work, we photolithographically pattern the highest energy density microbatteries at the picoliter (10^{-12} L) scale demonstrated to date, for the purpose of powering robotic devices on the microscale.

A major motivation behind this trend of shrinking the size of robots is to unlock applications inaccessible to larger devices.[6,9] A smaller size also enhances the mobility of sensors, enabling colloidal suspension of sensors and robots that can be carried along by fluid motion. To date, the majority of millimeter-scale sensors were either powered by solar cells[2-4,20] or did not have internal power sources.[21-24] However, to enable autonomous operation of colloidal robots in confined environments, such as pipelines, underground and *in-vivo*, on-board, high energy density units are required since access to ambient energy sources such as illumination are necessarily limited. Thus, there is a pressing need for integrating tiny batteries with the tiny sensors and robots.[12]

In this work, we demonstrate a facile route for fabricating and subsequently releasing microscopic Zn-air batteries with cleanroom techniques in a massively parallel manner. Utilizing dissolved oxygen, picoliter Zn-air batteries working in a neutral aqueous solution provided an energy density over 760 Wh L^{-1} (2.75 μJ pL^{-1}) and an areal power density of 0.15 mW cm^{-2}, with an open circuit voltage of 1.16 V. This represents the highest energy density for energy storage devices below 1 μL in volume. We find that due to the inherent high surface-area-to-volume ratio, picoliter batteries do not require special materials or sophisticated 3D structure to achieve high energy density and power density. When the batteries operate in phosphate-buffered solution, commonly employed to study physiological environments, the exposed Zn anode is shown to generate a zinc phosphate over-coating. This coating, however, does not impede the realization of high energy densities. We show that the batteries are able to switch on memristors and power actuators of similar sizes, demonstrating potential applicability to cell-sized autonomous robots. With linear dimensions ranging from 10 to 100 μm, they represent the first class of full-cell batteries capable of providing electricity to picoliter-sized machines.

Results

Design, Fabrication and Release of Picoliter Batteries:

Our approach differs fundamentally from those employed previously to create millimeter-sized batteries,[15,25] due to the requirement of direct integration with microscopic loads through photolithography, which is challenging to achieve with post-fabrication assembly methods.[12,26] As mentioned above, conventional battery materials are prepared using wet chemical methods, such as slurry casting, which are fundamentally incompatible with microelectronic fabrication processes.[12] This has apparently limited microbatteries to millimeters in size in the literature,[13-16] which is 1,000,000 times larger in volume than the target load devices for emerging micro-robotics.[26-28] Similarly, the usage of organic liquid electrolytes is another hurdle for fabrication, release and biomedical applications.[29-33] All-solid-state Li-ion batteries have been demonstrated with solid electrolytes,[34 35-37] though the deposition of such ceramic materials is usually extremely slow (<0.01 nm s^{-1}). Nevertheless, the high air and moisture sensitivity of anode materials (such as Li metal or LiC_x) and electrolytes complicates the fabrication processes, requiring hermetic sealing which would inevitably expand the device volume for micro-robotic applications.[32,33] As a result, picoliter-sized full-cell Li-ion batteries that can be integrated with microscopic robotic components have not been demonstrated to date.

Zn as an anode material possesses high stability under ambient conditions, which allows for a high deposition rate (> 1 nm s^{-1}) and facile integration with standard photolithography processes. We selected Zn-air chemistry because theoretically it provides very high specific energy (1350 Wh kg^{-1}) and energy density (>6000 Wh L^{-1})[38-40] which are essential metrics for micro-robotic applications. Unlike other Zn-based batteries,[41-62] in practice, primary Zn-air batteries also provide an impressive energy density of 1100 Wh L^{-1} (Supplementary Table 1),[63,64] much higher than rechargeable Li-ion batteries. We note that Zn is also compatible with physiological environments.[65,66] Examples of Zn-air microbatteries in the literature to date[63,64,67-73] are millimeters in scale and are not suited for mass production nor parallel release from a substrate, suggesting incompatibility with colloidal robotics.

To scale Zn-air batteries down to the picoliter regime and to make them a modular component of microscopic machines, we have designed a planar configuration as shown in Fig. 1a to 1c. A typical device consists of a 40 μm × 50 μm Zn anode and a Pt cathode of the same size, both sitting on a polymer base of 100 by 100 μm (Fig. 1c). Smaller devices have also been fabricated. As an aqueous ionic environment is typical for micro-robotic applications, an electrolyte does not have to be incorporated during fabrication (Fig. 1a). This approach has been previously employed on millimeter-scale devices, and was proven to be effective in simplifying the fabrication procedure.[69,72,74] More importantly, harnessing both the cathodic material (O_2) and the electrolyte from the environment drastically improves the energy density, which is critical for reducing the size of colloidal robots. With standard photolithography, 10,000 batteries (a 100 × 100 array) of the same design can be fabricated on a single 2 inch wafer shown in Figure 1d. We verified that at least 98% of the electrode pads are intact after fabrication, with resistance less than 100 Ω (Supplementary Fig. 1a). By randomly sampling 134 devices across several wafers from different batches, we estimated the average open circuit voltage of the entire population to be 1.05 ± 0.02 with 95% confidence level (Supplementary Fig. 1b), and the 95% confidence interval of the population standard deviation to be 0.108 to 0.137 V. First, SU-8 polymer (2 μm thick) was cross-linked by contact photolithography to form a chemically stable, mechanically strong and electrically insulating base (Fig. 1e) with a customizable thickness (Supplementary Fig. 2). Second, the platinum cathode was patterned and evaporated together with the current collector for the anode (Fig. 1f). From bottom up, the Pt cathode consists of a Ti (or Cr) adhesion layer, a Ag layer for mechanical flexibility, a second adhesion layer, and a functional layer of Pt. Finally, the pattern for the Zinc anode was defined and a Ti adhesion layer was sputtered (Fig. 1g). Metallic

Zn up to 1.5 μm thick (Supplementary Fig. 3) was deposited by thermal evaporation to complete the battery (Fig. 1h).

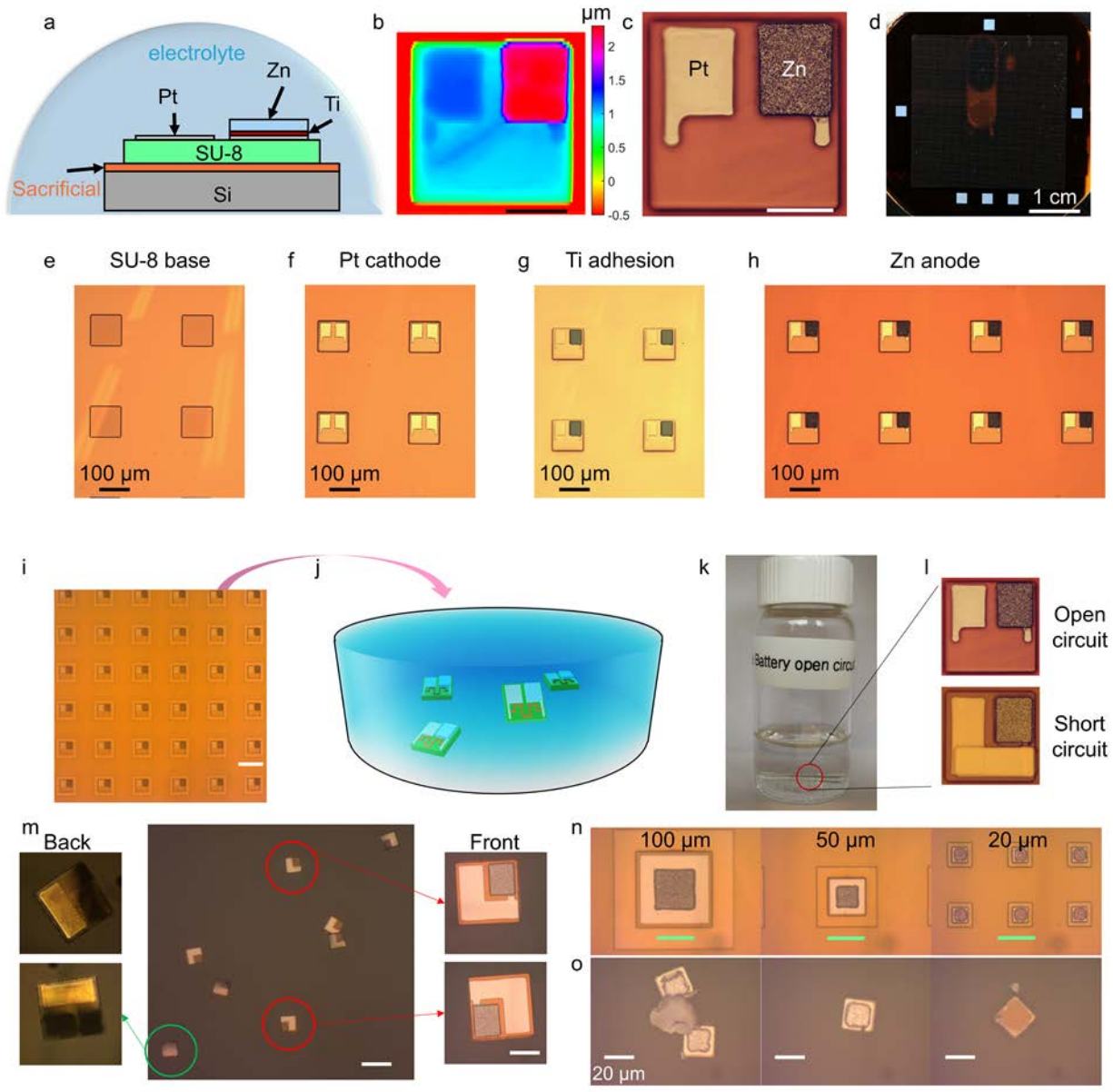

Fig. 1 | Fabrication and release of Zn/Pt/SU8 picoliter Zn-air batteries. a, Side view schematic of a Zn-air picoliter battery placed in a droplet of electrolyte. **b,** Height profile and **c,** optical micrograph of an open-circuit Zn-air picoliter battery after fabrication. Scale bar: 40 μm. From a to c, the SU-8 base has a side length of 100 μm. **d,** Image of a Si wafer with a 100 × 100 array of picoliter batteries. **e, f, g, h,** Optical micrographs of picoliter batteries at different stages of the fabrication, as indicated by the annotation. **i**, Optical micrograph of picoliter battery arrays patterned for Cu etching. Scale bar: 200 μm. **j,** Schematics of batteries with loads (memristors in this case) released into solution. **k,** Image of a bottle of dispersion containing 100 μm batteries. **l,** Optical micrographs of open circuit and short-circuited Zn-air picoliter batteries, both are 100 μm. **m,** Central image: optical micrographs of picoliter batteries deposited onto a

glass slide. Scale bar: 200 μm. Side images: optical micrographs of individual batteries that were facing down (left), and up (right). Scale bar: 50 μm. **n,** Optical micrographs of short-circuited batteries with various sizes. Scale bar: 50 μm. **o,** Optical micrographs of 20 μm batteries after releasing and re-depositing onto a glass slide. The dust in the leftmost image was residual from the sacrificial substrate. The rightmost image showed a 20 μm battery that was facing downward.

To enable facile release of microbatteries into solution, we fabricated them on a sacrificial substrate comprising a photoresist/Cu bilayer (Fig. 1a). After fabrication, a frame was patterned around each battery (Fig. 1i), where the Cu was etched away (Supplementary Fig. 4), and the photoresist was dissolved to release the batteries (Fig. 1j). The batteries can be stored in various solvents (Fig. 1k), such as THF and acetonitrile, for over 3 months. In addition to the open-circuit design in Figure 1a, we also fabricated short-circuited ones where the Pt and Zn electrodes were connected (Fig. 1l, Supplementary Fig. 5). When the aged dispersion was transferred onto glass slides and dried, over 90% of the batteries were observed to have an intact appearance (Fig. 1m). Almost all of them appeared flat, the probability of the front side facing up was close to 50% (Fig. 1m, Supplementary Fig. 6). Short-circuited Zn-air batteries smaller than 50 μm were also produced, for which we adopted a design with Zn sitting at the center on top of the Pt (Fig. 1n). This configuration requires lower fabrication accuracy and resolution, facilitating the downscaling of device sizes. The 20 μm batteries can be released and remain intact after transferring onto slides (Fig. 1o), although the yield of release was much lower than the 100 μm devices (Supplementary Fig. 8). By measuring the amount of Cu^{2+} ions displaced by Zn metal in a mixture of battery dispersion and copper(II) chloride solution (Supplementary Fig. 9), the thickness of Zn was verified to be consistent with that acquired by profilometry.

Performance of Picoliter Batteries:

To characterize the electrical performance of these tiny batteries on a probe station, we have fabricated some devices with extended leads (Supplementary Fig. 10). We connected one probe with each electrode through the leads to monitor the voltage and current of our batteries (Supplementary Fig. 10g). A drop of pH-neutral electrolyte solution was added onto the device to emulate an operating environment for released picoliter batteries.[66] The active device exposed to the electrolyte had exactly the same design as the picoliter batteries in Fig. 1c, while the wires were covered by a layer of insulating SU-8 to prevent any interference with the measurements (Supplementary Fig. 10c). The amount of electrolyte was in large excess (>10 μL) compared to the device volume, in order to minimize the effect of water evaporation. Batteries of various electrode sizes were fabricated on a sacrificial substrate, so that they can undergo a release procedure similar to that experienced by batteries without wires (Supplementary Fig. 10d-f).

Galvanostatic discharge of picoliter batteries was conducted in neutral electrolytes with 0.15 M of various salts (Supplementary Fig. 11). Batteries in phosphate-buffered saline (PBS) showed significantly higher voltage and capacity compared to those in other electrolytes (Figure 2a), despite a higher discharge rate. In PBS, identical picoliter Zn-air batteries were able to deliver over twice as much energy and power as in other electrolytes (Figure 2b). Meanwhile, the fluctuation of voltage in PBS was much more noticeable than that in any other solution (Figure 2a). The PBS solution contains NaCl, KCl, KH_2PO_4 and Na_2HPO_4. Since neither control experiments with NaCl or KCl solutions was able to replicate the performance in PBS, the phosphate buffer pair should be responsible for the superior energy and power. Inspection of the batteries after discharge revealed the existence of inorganic coatings on the Zn electrode in PBS, which was not observed in any other electrolyte (Figure 2c, Supplementary Fig. 12). We identified the product as zinc

phosphate formed by the following reactions in PBS, distinct from those for conventional Zn-air batteries, shown in Fig. 2d:

$$\text{Cathode: } O_2 + 2\ H_2O + 4\ e^- \rightarrow 4\ OH^-$$

$$\text{Anode: } 3\ Zn + 2\ OH^- + 2\ HPO_4^{2-} \rightarrow Zn_3(PO_4)_2 + 2\ H_2O + 6\ e^-$$

$$\text{Overall: } 6\ Zn + 3\ O_2 + 4\ HPO_4^{2-} + 2\ H_2O \rightarrow 2\ Zn_3(PO_4)_2 + 8\ OH^-$$

On the cathode, Pt catalyzes the reduction of oxygen to form hydroxide ions, which is the same as in Zn-air batteries with the other tested electrolytes. On the anode side, instead of reacting with water to form zinc hydroxide, Zn^{2+} reacts with phosphate ions (PO_4^{3-}) to form a precipitate, and the hydroxide ion from the cathode is buffered by HPO_4^{2-}. This mechanism is consistent with previous reports on macroscopic Zn-air batteries using similar electrolyte.[75]

The reaction mechanism above was confirmed by energy dispersive X-ray spectroscopy (EDS) and X-ray powder diffraction (XRD) characterization of the discharge product in PBS. Most peaks in the XRD spectrum were assigned to zinc phosphate tetrahydrate (Fig. 2e). Quantitative analysis of the EDS spectra revealed an Zn:P:O atomic ratio of about 3:2.3:13 (Fig. 2f), consistent with the chemical composition determined by XRD. The EDS mapping showed a uniform distribution of Zn, O and P across the particles (Fig. 2g), suggesting a homogeneous composition. The discharge product is likely a mixture of amorphous and crystalline components, as e-beam diffraction showed no discernible structure for most regions probed, while the XRD results clearly demonstrated crystallinity. Based on this evidence for a $Zn_3(PO_4)_2$ layer, our observed voltage fluctuations are attributed to stochastic pitting corrosion of the Zn anode.[76,77] In PBS, $Zn_3(PO_4)_2$ will precipitate at a lower Zn^{2+} concentration than $Zn(OH)_2$ (Fig 2e-g, Supplementary Note 2), which is the main precipitate in the other neutral electrolytes tested. As a result, a thicker, more continuous and less permeable passivation layer forms on Zn during galvanostatic discharge in the PBS electrolyte, leading to more dramatic voltage fluctuations when pitting corrosion occurs. The mechanical disturbance generated by the growing zinc phosphate film may also contribute to the voltage fluctuations. We also noted that the voltage fluctuations of our battery are larger than in the literature due to the smaller size and the lack of an ion-exchange polymer coating.[75] A picoliter battery is expected to have a larger fluctuation than a macroscopic one, because the inhomogeneity of the electrode material plays a larger role on a smaller area. However, the higher overall power and energy density we observe in PBS compared to in other electrolytes indicates that this passivation layer reduces the self-discharge of the Zn anode. The fluctuation in the first 2000 s of discharge is typically less than 100 mV, which is about 10% of the OCV. More importantly, we have demonstrated that the battery is capable of providing reliable power to many types of micro-robotic loads.

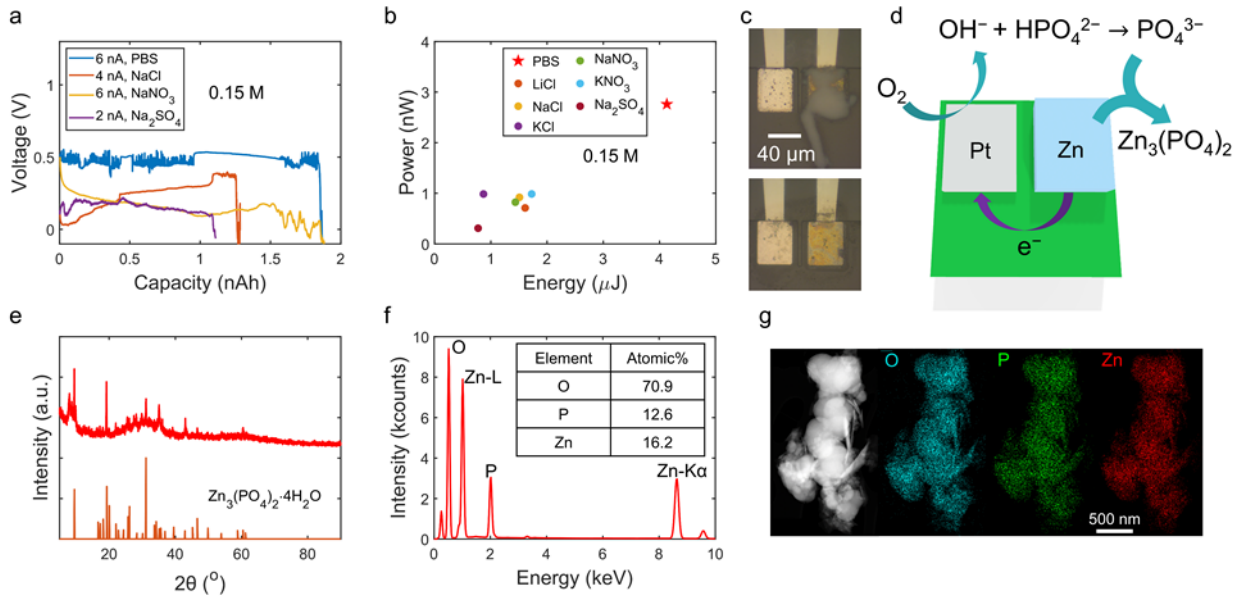

Fig. 2 | Reaction mechanism in picoliter Zn-air batteries. a, Galvanostatic discharge curves of picoliter Zn-air batteries in several representative electrolytes. **b,** Power versus energy plot (Ragone plot) extracted from galvanostatic discharge of picoliter batteries in various electrolytes. The concentration of cations was 0.15 mol/L in all electrolytes except PBS. The current of discharge was the highest possible value for the voltage to be positive in each electrolyte, which was 2 nA in sodium sulfate, 4 nA in lithium/sodium/potassium chloride, and 6 nA in sodium/potassium nitrate and PBS. **c,** Optical micrographs of picoliter batteries after galvanostatic discharge in PBS (upper) and LiCl (lower). **d,** Schematics of the half reactions and the overall reaction. **e,** XRD spectrum of the discharge product and the reference spectrum of hydrated zinc phosphate (Hopeite). **f,** EDS spectrum of the discharge product in PBS solution, with atomic percentage of the major elements, acquired with a scanning transmission electron microscope (STEM). **g,** High-angle annular dark-field (HAADF) image and the energy dispersive X-ray spectroscopy (EDS) mapping of the discharge product in the same region where EDS spectrum was collected.

Encouraged by the exceptional performance, we further studied these picoliter Zn-air batteries in PBS electrolyte. Voltage curves were measured by discharging the batteries at increasing current densities (per cathode area) from 0 to 0.75 mA cm^{-2}. Data were collected from 9 individual batteries (Fig. 3a) and averaged. The voltage monitored over 60 s at each current density was shown in Fig. 3c, and the time-averaged voltage versus current curves (polarization curves) were obtained as in Fig. 3b. The open circuit voltage of these batteries was around 1.2 V, and the short circuit current was about 10 nA (0.5 mA cm^{-2}). When we plotted the average voltage versus the normalized current (Fig. 3b, Supplementary Fig. 13), we found that the polarization curves were mostly invariant with respect to size. This indicates that the cell resistance scales with the size of the electrode, and the oxygen transport on the cathodic side is likely the rate-determining step. This is further supported by literature results that the discharge current scaled linearly with the cathode area when the Zn area was fixed.[78] This is also consistent with a much higher current density of oxygen reduction reaction (ORR) when the catalyst was loaded on a rotating ring-disk electrode,[79,80] or at the triple phase boundary,[38-40] where the transport of oxygen was greatly enhanced compared to our setup. We therefore normalize the current and power based on the *cathode area*.

Figure 3d-g shows the long-time galvanostatic discharge data of the picoliter batteries in PBS with various current densities. The thickness of Zn was supposed to be 700 nm based on the quartz balance in the deposition chamber, while the actual thickness measured by the profilometer was 1 μm, likely due to the loose packing of Zn micro-crystals. The average voltage dropped from about 0.5 V (Fig. 3d) to 0.3 V (Fig. 3g), while the average output power increased from 1 nW to near 3 nW (Fig. 3h), as the discharge rate increased from 0.1 mA cm^{-2} (0.24 C) to 0.4 mA cm^{-2} (0.96 C). This trend (Fig. 3h) was consistent with the voltage-current relationship obtained in the previous experiment (Fig. 3b). The fluctuating voltage observed in Fig. 2a was also seen here under various discharge rate. It is interesting to note that the duration of discharge did not decrease accordingly, but stayed roughly around 2000 to 3000 s (Fig. 3d, e, and g), with an exception at 0.3 mA cm^{-2} (Fig. 3f). This corresponds to an increase in capacity from 1/6 to over 50% of the theoretical value (30 μC) as the discharge accelerated (Fig. 3i), which is opposite to the common trend in most batteries. Self-discharge may explain the limited operation time of the Zn anode, leading to lower capacity at lower discharge rates. The discharge product growing on the surface of the Zn anode could eventually block its access to the electrolyte, which might also lead to a premature failure (Supplementary Fig. 14). However, some exceptions do exist at high rates (above 0.3 mA cm^{-2}) with close-to-theoretical capacity (blue curve in Fig. 3f and yellow curve in Supplementary Fig. 15d), which did not exhibit self-discharge for a much longer time (>4000 s). The released batteries with wires delivered one-third less capacity compared to batteries tested on wafer (Supplementary Fig. 16), due to damages of the Zn electrode during the release and transfer process which involved a series of mechanical manipulation and repeated solvent washing. Aging of the batteries in the solvent for more than 1 month does not appear to lead to failure of the picoliter batteries (Supplementary Fig. 15e-f).

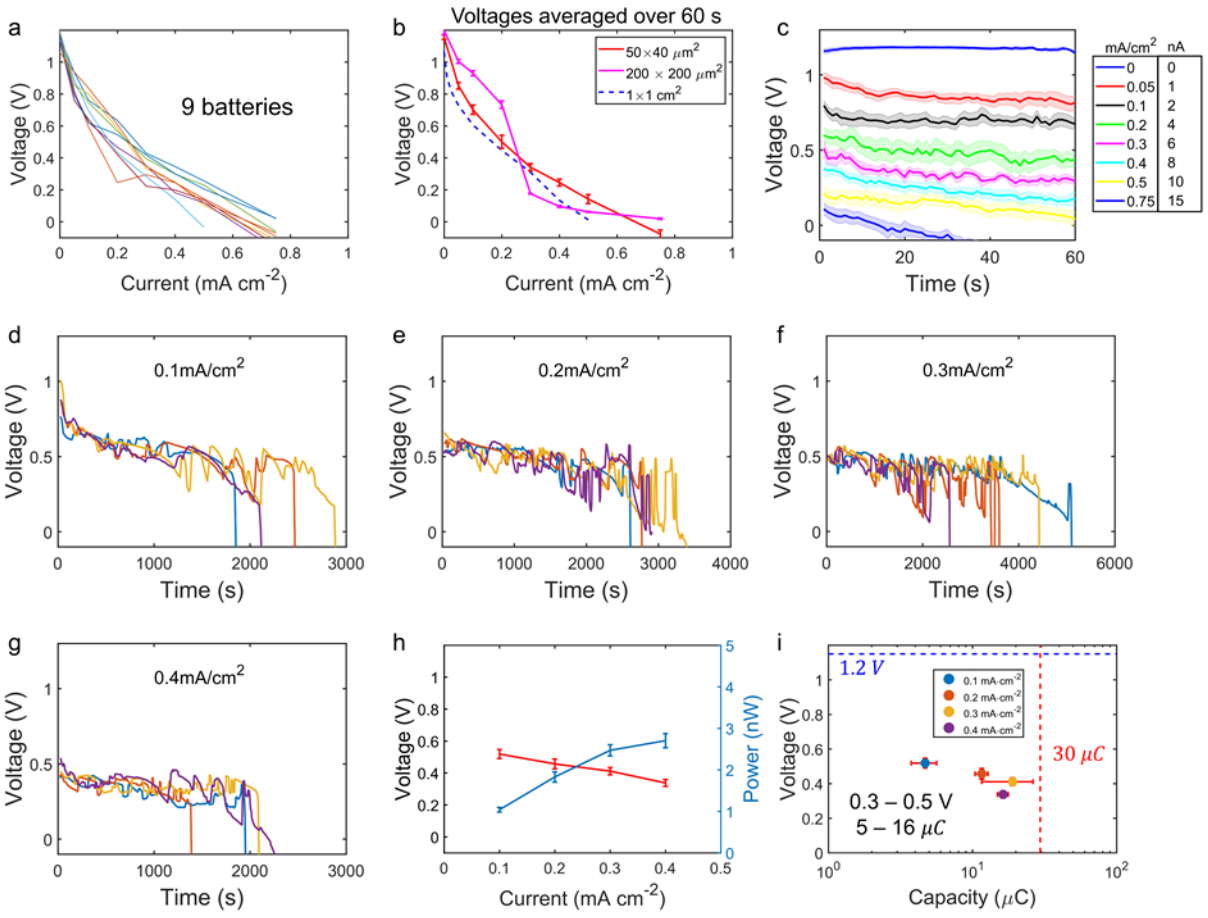

Fig. 3 | Performance of picoliter Zn-air batteries in PBS. a, Polarization curves of 9 individual batteries with 50 μm × 40 μm electrodes. **b**, Polarization curves from batteries of three different electrode areas. **c,** Voltage versus time curves for Zn-air picoliter batteries under different discharge current densities, the shaded regions indicate the standard error of the measurement. The legend shows the correspondence between actual current and current density normalized by the area of Pt electrode. **d-g,** Galvanostatic discharge curves of picoliter Zn-air batteries under current densities of **d**, 0.1 mA cm^{-2}, **e**, 0.2 mA cm^{-2}, **f**, 0.3 mA cm^{-2}, and **g,** 0.4 mA cm^{-2}. Data from 4 devices are shown for each rate, more discharge curves can be found in Supplementary Fig. 13 and 16. These batteries have 1 μm thick Zn and a volume of 2 pL. **h,** Polarization curve and power curve by averaging the galvanostatic discharge curves in Fig. 3d-g. **i,** Average voltages and capacities of batteries under 4 current densities. The theoretical capacity and open circuit voltage are indicated by the dashed lines.

A Ragone plot of the individual performance of each tested battery shows reasonable consistency across devices under the same testing condition (Fig. 4a). Unlike the commonly observed negative correlation between energy and power densities (red squares in Fig. 4b), there appeared to be a somewhat positive correlation for our picoliter Zn-air batteries. This is due to the self-discharge effect discussed in the previous paragraph. Because the cathodic reactant O_2 came from the solution environment, the net volume of the battery (2 pL) was dominated by the Zn anode, while the Pt cathode accounted for less than 10% of the volume. The total output energy of one picoliter battery was about 5.5 μJ at 0.4 mA cm^{-2}, which translates to an energy density of 2.75 μJ pL^{-1} (~760 Wh L^{-1}). At 0.3 mA cm^{-2}, devices with exceptionally high energy densities (near 6 μJ pL^{-1}) give rise to a higher average of 3.85 μJ pL^{-1} (1070 Wh L^{-1}). Compared to Li-ion microbatteries reported in the literature,[13-16,25,32,36,37,81-83] our Zn-air battery benefits from harvesting part of its reactants from the environment, hence offers a higher energy density among other advantages (Fig. 4c), despite its simple structure and facile fabrication. More importantly, it has a volume 5 orders of magnitude smaller than almost all microbatteries in the literature. Therefore, we have demonstrated the first picoliter battery that has appreciable energy density and can be fabricated with standard photolithography, which makes it a promising energy source for cell-sized robots and sensors.[6-8]

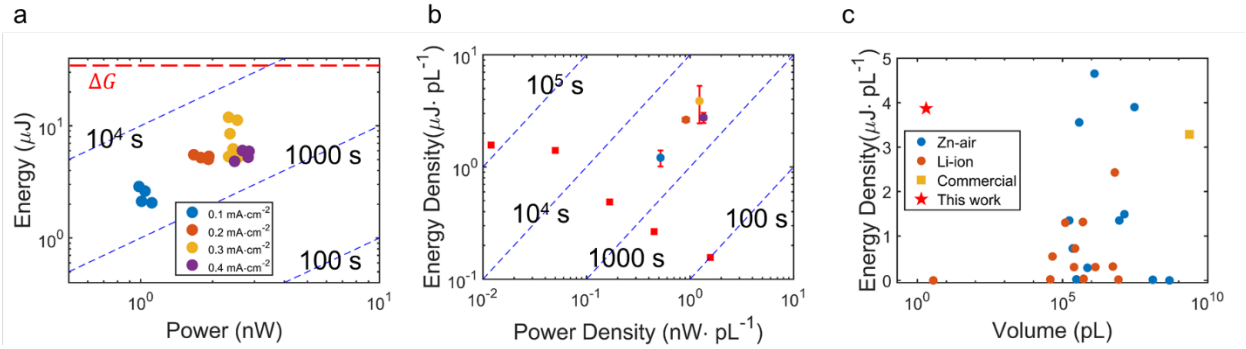

Fig. 4 | Performance summary and comparison. a, Ragone plot of energy and power of individual batteries with 2 pL volume, the data were calculated from Fig. 3d-g. The theoretical Gibbs free energy of the cell reaction is shown as the red dashed line. **b,** Ragone plot of the average energy and power densities under 4 current densities. The error bars represent the standard deviation across multiple devices. The red squares are data of Li-MnO_2 primary microbatteries from literature.[84] **c,** Master plot of the energy density versus cell volume for various microbatteries reported in the literature (electrolyte volume excluded for all entries). This work is shown in red asterisk.

Powering Micro-Robotic Loads

Memristors are two-terminal devices whose resistance is modulated based on the history of current passing through. We have used memristors in the past for information storage on a colloidal state machine with a relatively simple structure.[8,9] In this work, commercial memristors purchased from Knowm Inc. were connected with picoliter batteries in a setup shown in Supplementary Fig. 25a. The cyclic voltammetry curves of the memristors (Supplementary Fig. 25c) show that they can be switched from an off state with 1 GΩ resistance to an on state with 1 to 10 MΩ resistance at a threshold voltage of around 0.2 V, making them suitable loads for our picoliter batteries. Fig. 5a shows that after 20 minutes of discharging, a memristor can be successfully turned on by a Zn-air battery of only 2 pL volume. Compared to the control devices which remained in the off state, devices that were connected to the batteries exhibited significant increase in conductance of up to 3 orders of magnitude (Fig. 5b). The relatively large variation in the final on-state conductance is attributed to variabilities of both the batteries (Fig. 3) and the memristors (Supplementary Fig. 25), and was likely magnified by the nonlinear switching characteristic of the memristors. Nevertheless, all devices showed on-off ratios larger than 3, which was an obvious change in the I-V curves (Supplementary Fig. 26). In comparison, the control samples had almost no increase in the conductance (on-off ratios less than 1.5). This experiment confirmed the capability of picoliter batteries to power microscopic electronic devices. The memristors have a dimension of around 50 μm, hence could potentially be integrated with our batteries to enable the construction of fully autonomous colloidal robots.[85]

Recently, Miskin et al. demonstrated Pt-Ti bilayer metallic actuators as legs for microscopic robots.[7] Bias voltages applied on the actuator caused the adsorption/desorption of hydrogen or oxygen species on the Pt surface,[7] which changed the stress distribution and the curvature of the device (Fig. 5c). Once connected with the Zn electrode of the battery, the actuator bent from its flat state (50 μm long, 12 μm wide) to a maximum curvature of around 0.1 μm^{-1} in about 4 s (Figure. 5d-e, Supplementary Video 1). When we reversed the bias by connecting the Pt cathode of the battery with the actuator, it relaxed to the flat state at a similar rate. The response time is in agreement with the RC constant of the circuit (Supplementary Note 4). We showed that another 60 μm × 14 μm actuator could be powered by a 1.6 pL battery to quasi-reversibly bend and flatten over 50 cycles (Supplementary Fig. 27, Supplementary Video 2). After prolonged operation, a decay in the minimum curvature (maximum actuator length) was observed (Figure. 5d-e, Supplementary Fig. 27b-c), accompanied by a slowing down of the flattening response time to over 10 s. Meanwhile, the maximum curvature as well as the curling response time remained almost unchanged. This was possibly due to some irreversible changes of the actuator during repeated actuation under high voltage,[86] as evidenced by the difficulty to flatten it afterwards (Supplementary Fig. 28 and Supplementary Video 3). The total current passing through the actuator consisted of a pulse component from capacitive discharge and a constant part from Faradaic current, as shown in Fig. 5f. It is estimated that about 60% of the battery's total energy was consumed by the actuator (Supplementary Note 4), mostly to drive the Faradaic reactions. The disparity between the positive and negative Faradaic currents is explained by a difference in the reduction and oxidation reaction rates on the actuator.

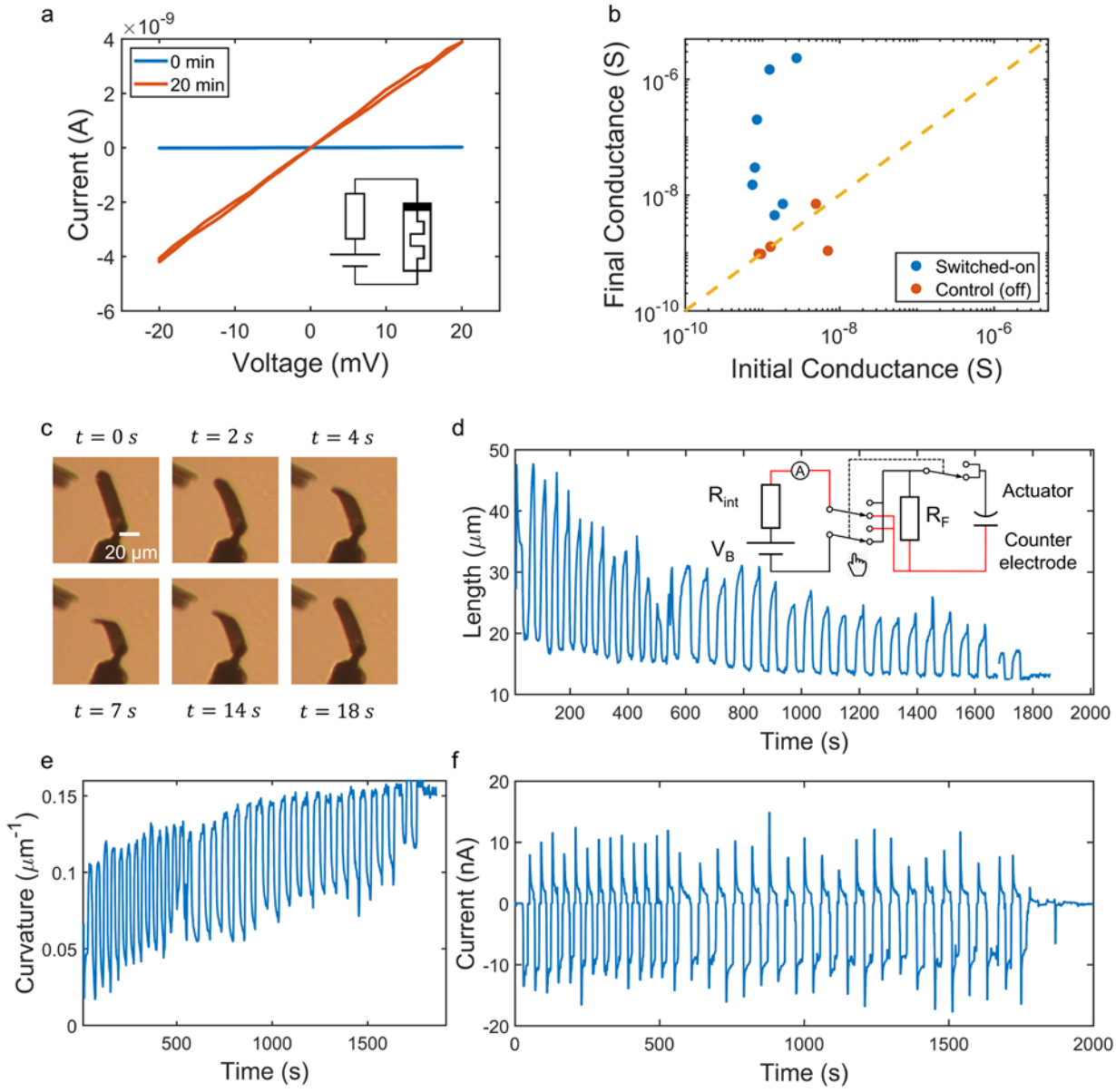

Fig. 5 | Application of Zn-air batteries. a, Current-voltage (IV) curves of a memristor connected with a 100 μm picoliter battery (2 pL) before and after 20 min of discharging in PBS electrolyte. The batteries are from the same batch of devices used for performance characterization in Fig. 3. The inset shows the schematic of the circuit. IV curves of other switched-on devices can be found in Supplementary Fig. 26. **b**, Scatter plot of the initial and final conductance of memristor devices that were switched on by batteries (blue) versus those not powered (orange). **c**, Images of a Pt-Ti surface electrochemical actuator (SEA) curling and flattening under cyclic voltammetry measurement with 0.4 V amplitude. A platinum wire was used as the counter electrode. The curvature of the actuator increased when sweeping towards negative bias, and decreased when sweeping towards positive. The curvature of the actuator increased when sweeping towards negative bias, and decreased when sweeping towards positive (Supplementary Fig. 28). **d**, Length of a 50 μm × 12 μm SEA over 35 cycles of actuation powered by a 1.6 pL battery. The battery was in a separate solution from the SEA. The inset shows the circuit diagram used in this experiment. **e**, Curvature

of the actuator during operation converted from the length shown in **d**. **f**, Current recorded by an ammeter during the actuation shown in **d**.

Sensors are essential components for the autonomous operation of a micro-robot, hence we have further demonstrated the capability of our picoliter battery by powering resistive chemical sensors. In Fig. 6a-b, two chemical sensors made of different materials were both successfully powered by picoliter batteries. When a water droplet containing the analyte triethylamine (TEA) was added onto the monolayer MoS_2 sensor, the impedance of the device decreased thus the output current of the battery increased significantly (Fig. 6a).[8] The other sensor based on single-walled carbon nanotube (SWNT) was less sensitive than the MoS_2 sensor, requiring higher analyte concentration and rendering smaller signal, but still produced a clear change in the output current (Fig. 6b). Note that neither devices were optimized for this application. Nevertheless, their response ($\Delta I \sim 20$ nA) were large enough to drive at least some potential loads, such as the aforementioned memristors and actuators. The very large current means that the on-state resistance of the MoS_2 sensor is negligible compared to the internal resistance of the battery or the resistance of a bimorph actuator. Therefore, if an actuator and a sensor are connected in series, a battery is essentially directly powering the actuator when the sensors are turned on. If paired with memory devices, our batteries could provide the energy necessary to record environmental information as non-volatile memory in the form of resistance change to be recovered later.

Lastly, our batteries also enabled a basic and key function for all autonomous machines, which is a clock signal generator. Using a simple relaxation oscillator (Fig. 6c) composed of a picoliter battery, a resistor (1 GΩ), a capacitor (4.7 nF) and two commercial CMOS inverters (SN74HC04), we managed to generate a regular AC signal. The amplitude of the signal had some variation over time due to the voltage fluctuation of the battery, but a stable frequency of 0.1 Hz was maintained over the entire discharge period (Fig. 6d). Such a stable, low-frequency clock signal would enable the micro-robot to keep track of time and perform sequential logic operations.[87] More efficient oscillator design and much more complex micro-chiplet circuits have already been demonstrated in the literature (Supplementary Table 2), most of which require power on the order of nW when in standby mode (not performing data transmission). Overall, we have demonstrated the ability of the picoliter batteries to drive 5 different applications, including a memristor, an actuator, 2 types of sensors, and one oscillator circuit. Building onto these capabilities, in the future we plan to explore the possibilities of creating autonomous cell-sized robots capable of self-powered sensing, steering and locomotion.

It is worth mentioning that since many of our targeted loads, such as the bimorph actuator and the sensors, need to work in an aqueous environment, the integration of a picoliter Zn-air battery with those loads is expected to be easy and natural. Other loads that might be sensitive to liquid, such as some microelectronic circuits, need to be encapsulated anyway in order for the colloidal robots to work in solution. Therefore, the integration of a battery with those encapsulated loads will not be a problem either.

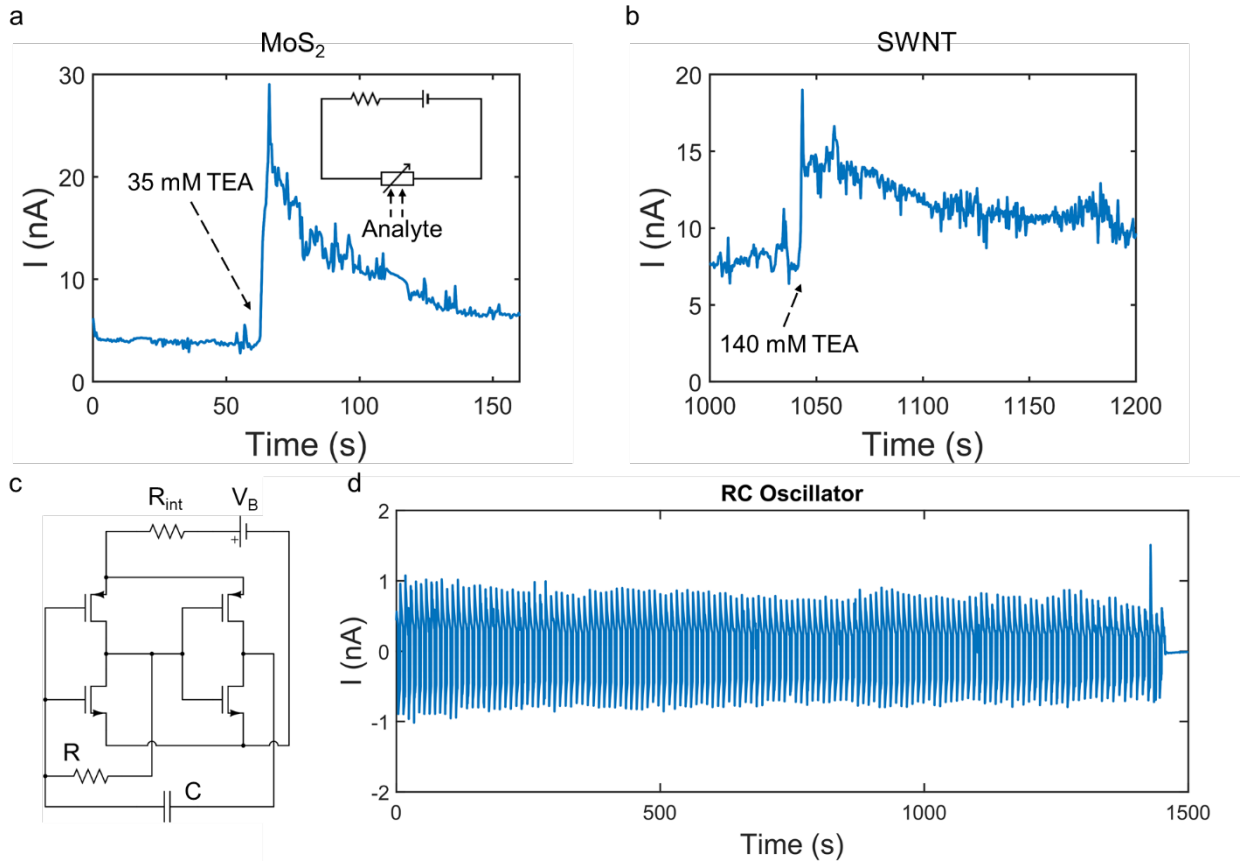

Fig. 6 | Application of Zn-air batteries continued. a, Current response (IV) curves of an MoS_2 chemiresistor connected with a picoliter battery (2 pL) during the addition of a droplet containing 35 mM TEA. **b**, Current response (IV) curves of a SWNT chemiresistor connected with a picoliter battery (2 pL) during the addition of a droplet containing 140 mM TEA. **c**, Circuit diagram of an RC oscillator with two inverters powered by a picoliter battery. **d**, Current signal of the RC oscillator over 1500 s.

Conclusion

Compared to other microbatteries reported to date, the Zn-air picoliter batteries reported in this work offer one of the highest energy densities (Fig. 4c), but their power density has significant room for improvement (Supplementary Fig. 29). We note in particular that increasing the power density is helpful for performing tasks like locomotion and communication (Supplementary Table 2). Improvements will therefore enable significant increases in capability and task flexibility for microscopic sensors and robots. We have identified the cathodic reaction, or more accurately the transport of O_2, as the rate-limiting step in this system. Hence the easiest next improvement is to increase the area of the Pt cathode. However, the size of Pt is constrained by the projected area of the device to be powered, while increasing the specific area is ineffective. Alternatively, we may increase the access to oxygen by creating triple phase boundaries, which may require polymer/gel electrolyte compatible with photolithography. Replacing the Pt with other types of cathode, such as Ag_2O, MnO_2 and NiOOH may remove the limitation of O_2 in solution (Supplementary Fig. 30a-c), and may lead to rechargeable picoliter batteries. To mitigate the large voltage fluctuation towards the end of discharge, a larger discharge rate or a conformal polymer coating on Zn may also be desirable (Supplementary Fig. 30d-f). In future works, we plan to explore Zn-based picoliter batteries with a higher power density and rechargeability.

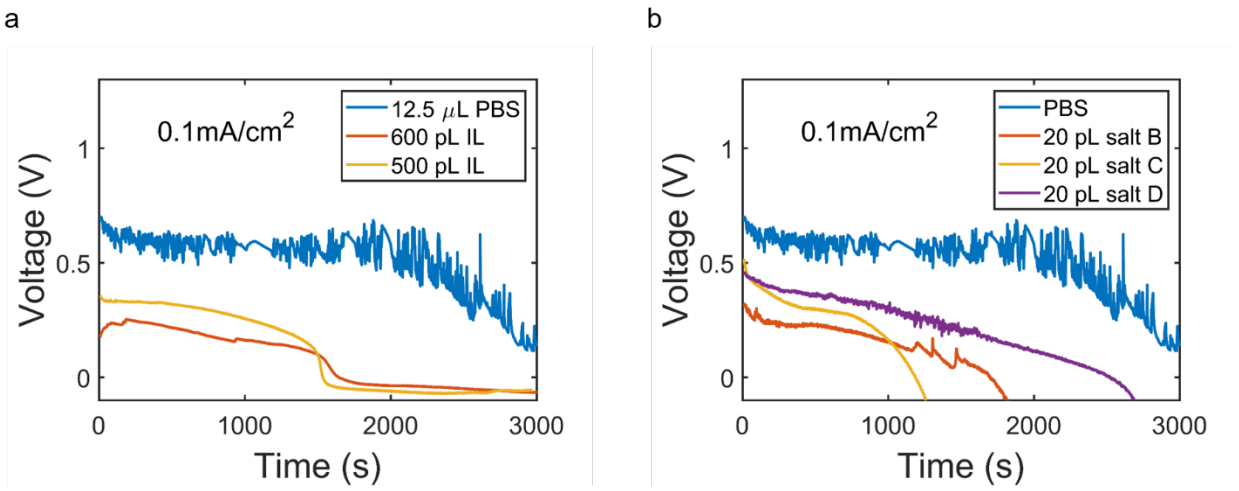

Fig. 7 | Alternative Picoliter Zn-air batteries designs for various application scenarios. a, Ionic-liquid-based batteries for applications that require a closed-battery configuration. Galvanostatic discharge curves of Zn-air batteries in 500 to 600 picoliter of ionic liquid under a current density of 0.1 mA cm^{-2}. The ionic liquid electrolyte is composed of 1 M $Zn(BF_4)_2$ in 1-Ethyl-3-methylimidazolium tetrafluoroborate ([EMIM][BF_4]). **b**, Semi-closed, salt-releasing batteries for applications in pure water. Galvanostatic discharge curves of Zn-air batteries carrying 20 picoliter of salt, under a current density of 0.1 mA cm^{-2}. The salt-carrying batteries were immersed in 10 μL of DI water.

Although our colloidal batteries are intended to operate in a large reservoir of electrolyte, there are other application scenarios where the micro-robots are in a dry environment, or where ionic species are not available in the liquid environment. To this end, we did two proof-of-concept experiments demonstrating the potential of picoliter Zn-air batteries. For the first scenario where a closed-battery is preferred, we used micro ink-jet printer to precisely drop 500 picoliter of ionic liquid electrolyte onto our batteries (Fig. 7a). The battery delivered 0.82 μJ of energy at a current density of 0.1 mA cm^{-2}. Although smaller than PBS-based batteries, the batteries with ionic liquid still delivered 1.6 nJ/pL of energy density (electrolyte volume included), which still outperform the smallest energy storage devices in the literature.[17] Further reduction of electrolyte volume and introduction of a box to seal the ionic liquid could allow for a self-contained picoliter-sized battery. In the second experiment, we added 20 picoliter of salt to the battery by drying a dilute electrolyte solution. When immersed in deionized water, the battery released salt and was able to deliver 0.6 to 1.2 μJ of energy at a current density of 0.1 mA cm^{-2} (Fig. 7b). This semi-closed, salt-releasing configuration ensures that the picoliter batteries can operate even without ions in the environment. Overall, these experiments show that the Zn-air batteries could potentially operate in different environments, and do not necessarily require an infinite electrolyte reservoir.

In summary, we have presented the fabrication, release, characterization and application of Zn-air picoliter batteries. Employing standard photolithography, thousands of picoliter batteries were fabricated on a single wafer at once, and were easily released into solutions. Batteries of various sizes were created, ranging from 10 to 100 μm across. The electrochemical performance of these batteries were characterized on a probe station by galvanostatic discharge. The performance achieved were in agreement with our expectation, with an open circuit voltage of 1.2 V, a short circuit current density of about 0.5 mA cm^{-2} (10 nA/2000 μm^2), a power of 0.15 mW cm^{-2} (3 nW/2000 μm^2) and a capacity of 300 mAh g^{-1} (16 μC/2 pL). Notably, our picoliter batteries demonstrated a remarkably high energy density of up to 1070 Wh L^{-1}, exceeding most microbatteries to date. Lastly, the tiny batteries were proven to be able to turn on memristors and drive actuators of comparable sizes. The high energy density, perfect compatibility with photolithography, and

relatively simple fabrication process make picoliter Zn-air batteries a desirable power source for colloidal electronics. As the first of its kind, this work should inspire more effort towards picoliter-scale energy storage and harvesting devices, and greatly expand the functionality and application of cell-sized robots and sensors.

Methods

Picoliter batteries fabrication. A layer of LOR-3A lift-off resist was first spin coated onto 2 inch Si wafer at 2000 rpm. The coated wafer was then baked at 180 ºC for 4 min and 190 ºC for 20 min, to increase the stability of LOR-3A during fabrication. A layer of 70-nm-thick copper was subsequently deposited on top of the LOR-3A by DC magnetron sputtering (AJA International). This formed the sacrificial LOR/Cu substrate, enabling easy release of batteries in later experiments. During fabrication, the Cu layer will protect the photoresist from being dissolved in the lift-off solution (Remover-PG).

To define an insulating base for batteries, SU-8 2002 negative photoresist was first patterned by contact photolithography on an MA-6 mask aligner. After development, the cross-linked SU-8 structure was hard-baked at 120 ºC for 4 min to increase adhesion and reduce stress. In the second photolithography step, LOR-20B and Shipley S1805 photoresist was patterned to define the electrical contacts to both electrodes. Wafers with only 100 μm batteries were patterned by contact photolithography, while wafers with various sizes of batteries were patterned by direct laser writing in a maskless aligner (Heidelberg MLA-150). A tri-layer metal of 5 nm/20 nm/5 nm Cr/Ag/Cr (or Ti/Ag/Ti) was deposited by Denton electron-beam evaporator, followed by 25 nm of Pt deposited by either e-beam evaporation or DC sputtering. The lift-off process was performed in Remover-PG solution on a shaker to remove the photoresist and extra metal. The third step used the same photoresist as the second step to define the zinc anode pattern. Titanium adhesion layer (10 nm) was first sputtered, after which Zn metal was deposited by Key High thermal evaporator. The thickness of Zn was monitored by a quartz crystal oscillator in the evaporation chamber. The lift-off process was performed in Remover-PG on a shaker at room temperature. For Zn- Ag_2O batteries, the cathode material was deposited by reactive sputtering of Ag target in O_2/Ar plasma. Finally, Shipley S1818 was coated and patterned to protect Zn and define an etching frame around each battery.

The fabrication of batteries with wires for electrical characterization shared the same procedure as described above, except for an additional step before the last one. Here, another layer of SU-8 2002 was patterned after finishing the third step, to shield the wires from electrolyte while exposing the active region of the device. Some of the batteries with wires were fabricated on other insulating substrate such as SiO_2 or glass, and were tested without releasing.

Release procedure. The as-fabricated wafer was immersed into Cu etchant 49-1 for 2 min to remove Cu in the etching zone around each battery. The wafer was then washed with DI water and acetone to dissolve the S1818 photoresist. Subsequently, the wafer was immersed into 20 mL tetrahydrofuran (THF) for 3 to 4 hours, to dissolve the LOR sacrificial layer. After releasing most of the batteries, the wafer was taken out, and THF was evaporated to less than 5 mL. Optionally, the photoresist-containing solution was then diluted by adding fresh solvent (THF or acetonitrile) and taking out old solvent with a pipette. The resulting dispersion was then collected for future characterization.

The batteries with wires were also etched and washed in the same way as stated above. Then 2 μL of Poly(methyl methacrylate) (PMMA) e-beam resist were drop casted onto each device as a protection layer. After drying and annealing, the wafer was immersed into 2 wt% KOH solution to release the devices. The floating devices after releasing were fished with glass slides, and cleaned with DI water and acetone.

Characterization. Optical images of batteries were acquired with a Zeiss Axio Scope A1 microscope using objective lenses of various magnifications (5×, 10×, 50×, 100×). The height profile of the batteries were measured with a Bruker DektakXT profilometer using a 2-μm-radius diamond-tipped stylus. The UV-vis spectra of batteries in copper chloride solution was measured with a Shimadzu UV-3101PC spectrophotometer at wavelengths of 250 to 600 nm. The discharge product was collected from a macroscopic Zn-air cell in PBS solution, centrifuged and washed twice with DI water, and dried for further characterization. The dried powder was dispersed in isopropanol and loaded onto TEM grid for HAADF and EDS mapping in Titan Themis Z G3 Cs-Corrected STEM. The powder XRD was measured on PANalytical X'Pert Pro diffractometer.

Electrical characterization. Electrical performance measurements of picoliter batteries were performed in an ARS PSF-10-1-4 Cryogenic Probe Station using micromanipulators as probes. All measurements were done on batteries with wires in two-electrode configuration under ambient condition. One probe connected to the Pt electrode served as the working electrode, the other probe connected to the Zn electrode served as the counter and reference electrode. Voltage and current were applied onto the probes through a semiconductor parameter analyzer (SPA) (Agilent E5262A Source Measure Units, controlled by MATLAB code. Before measurement, a drop of PBS or other types of electrolyte (10 to 15 μL) was added onto the active region of the device. The droplet does not spread out to the probes due to a large contact angle with the SU-8 polymer. Voltage polarization curves were obtained by sequentially increasing the galvanostatic discharging current density from 0 to 0.75 mA cm^{-2}. The voltage was monitored for 60 s at each current density, with 20 s rest before the next measurement on the same device. Long-time galvanostatic discharge was carried out continuously until the voltage drops below zero for more than 1 min, where the battery was considered to be dead. Deionized water (4 to 8 μL) was added to compensate for the evaporation of water from the electrolyte droplet, if the discharge lasted for longer than 2000 s.

Short circuit discharge experiment. The bottle containing short-circuited picoliter batteries were agitated, and 10 μL of dispersion were drop casted onto a glass slide. After drying, a hydrophobic PMMA well was pipetted around the batteries by hand. The batteries on slides were observed continuously under a Zeiss microscope (50× objective) after adding 100 μL of PBS electrolyte, until the batteries are fully discharged. PBS electrolyte was bubbled with pure oxygen for 5 min to create oxygen-saturated solution. When using this solution, a rubber well and a thin glass cover slide were used to seal the volume, preventing gas exchange with ambient air. The oxygen level was measured by a RCYAGO dissolved oxygen meter.

Memristor switching experiment. Picoliter batteries with wires (Fig. 2a) and memristors were connected to probe needles respectively, and the needles were then connected through external cables. The initial resistance of memristors were recorded by semiconductor analyzer. After disconnecting the cables form the semiconductor analyzer, 12.5 μL of PBS electrolyte were added to the battery. The memristors were disconnected from the batteries 20 min later and the final resistance were recorded. For the control devices, we measured the resistance of a device at rest in the off state every 20 min.

Actuator experiment. Pt-Ti bimorph actuators were fabricated on a Cu sacrificial layer according to the procedure reported previously.[7] They were released by etching away Cu substrate in a 4 mg/mL ammonium persulfate solution overnight. The floating actuators were then transferred with the Si wafer into a petri dish with PBS solution. Individual actuators were picked up by parylene-coated Ir/Pt probes from Microprobes for Life Science. The actuators were first tested with 0.4 V amplitude cyclic voltammetry at a sweep rate of 73 mV s^{-1}, with a Pt wire as the counter and reference electrode. Then it is connected to a picoliter battery in a separate solution with external wires. The polarity of connection was switched to cause cycles of actuation by manually re-connecting wires at a regular pace, until the battery fully discharged and the actuation stopped. The state of the actuator was filmed in the meantime. For the recording of current, a

semiconductor parameter analyzer was connected in series with the battery and set to maintain a constant voltage of 0 V.

Sensor experiment. Picoliter batteries with wires and chemical sensors were connected to probe needles respectively, and the needles were then connected through external cables. Before starting the program, 12.5 μL of PBS electrolyte were added to the battery. For the recording of current, a semiconductor parameter analyzer was connected in series with the battery and set to maintain a constant voltage of 0 V. The chemical sensors were initially dry, after being powered for a few minutes, 1.5 μL droplet containing the analyte TEA was added onto the sensor.

Oscillator experiment. One picoliter battery with wires were connected to a resistor, a capacitor and two inverters through probe needles and cables according to the circuit in Fig. 6c. Before starting the program, 12.5 μL of PBS electrolyte were added to the battery. The current was recorded until the battery ran out of charge.

Data availability

All relevant data are included in the paper and Supplementary Information. The source data are available from the corresponding author upon reasonable request.

Reference

1 Kahn, J. M., Katz, R. H. & Pister, K. S. Next century challenges: Mobile networking for "smart dust". in *Proceedings of the 5th annual ACM/IEEE international conference on Mobile computing and networking*. 271-278 (IEEE, 1999).

2 Warneke, B. A. & Pister, K. S. An ultra-low energy microcontroller for smart dust wireless sensor networks. in *2004 IEEE International Solid-State Circuits Conference (ISSCC)*. 17.14 (2004).

3 Fojtik, M. *et al.* A millimeter-scale energy-autonomous sensor system with stacked battery and solar cells. *IEEE J. Solid-State Circuits* **48**, 801-813, (2013).

4 Wu, X. *et al.* A 0.04 mm^3 16nW wireless and batteryless sensor system with integrated Cortex-M0+ processor and optical communication for cellular temperature measurement. in *2018 IEEE Symposium on VLSI Circuits*. 191-192 (IEEE, 2018).

5 Brooks, A. M. & Strano, M. S. A conceptual advance that gives microrobots legs. *Nature* **584**, 530-531, (2020).

6 Cortese, A. J. *et al.* Microscopic sensors using optical wireless integrated circuits. *P. Natl. Acad. Sci. USA* **117**, 9173-9179, (2020).

7 Miskin, M. Z. *et al.* Electronically integrated, mass-manufactured, microscopic robots. *Nature* **584**, 557-561, (2020).

8 Koman, V. B. *et al.* Colloidal nanoelectronic state machines based on 2D materials for aerosolizable electronics. *Nat. Nanotechnol.* **13**, 819-827, (2018).

9 Liu, P. W. *et al.* Autoperforation of 2D materials for generating two-terminal memristive Janus particles. *Nat. Mater.* **17**, 1005-1012, (2018).

10 Liu, A. T. *et al.* Autoperforation of two-dimensional materials to generate colloidal state machines capable of locomotion. *Faraday Discuss.* 10.1039/D0FD00030B, (2021).

11 Liu, A. T. *et al.* Colloidal Robotics. *In revision*, (2021).

12 Zhu, M. S. & Schmidt, O. G. Tiny robots and sensors need tiny batteries - here's how to do it. *Nature* **589**, 195-197, (2021).

13 Tang, H. *et al.* Stress-actuated spiral microelectrode for high-performance lithium-ion microbatteries. *Small* **16**, e2002410, (2020).

14 Sun, K. *et al.* 3D printing of interdigitated Li-ion microbattery architectures. *Adv. Mater.* **25**, 4539-4543, (2013).

15 Pikul, J. H., Zhang, H. G., Cho, J., Braun, P. V. & King, W. P. High-power lithium ion microbatteries from interdigitated three-dimensional bicontinuous nanoporous electrodes. *Nat. Commun.* **4**, 1732, (2013).

16 Lai, W. *et al.* Ultrahigh-energy-density microbatteries enabled by new electrode architecture and micropackaging design. *Adv. Mater.* **22**, E139-E144, (2010).

17 Lee, Y. *et al.* Nano-biosupercapacitors enable autarkic sensor operation in blood. *Nat. Commun.* **12**, 4967, (2021).

18 Li, Y. *et al.* On-Chip Batteries for Dust-Sized Computers. *Adv. Energy Mater.* **12**, 2103641, (2022).

19 Qu, Z. *et al.* A Sub-Square-Millimeter Microbattery with Milliampere-Hour-Level Footprint Capacity. *Adv. Energy Mater.* **12**, 2200714, (2022).

20 Teran, A. S. *et al.* AlGaAs photovoltaics for indoor energy harvesting in mm-scale wireless sensor nodes. *IEEE Trans. Electron Devices* **62**, 2170-2175, (2015).

21 Funke, D. A. *et al.* Ultra low-power, -area and -frequency CMOS thyristor based oscillator for autonomous microsystems. *Analog. Integr. Circ. S.* **89**, 347-356, (2016).

22 Maksimovic, F. *et al.* A crystal-free single-chip micro mote with integrated 802.15. 4 compatible transceiver, sub-mw ble compatible beacon transmitter, and cortex m0. in *2019 Symposium on VLSI Circuits.* C88-C89 (IEEE, 2019).

23 Aiello, O., Crovetti, P. & Alioto, M. A sub-leakage pw-power Hz-range relaxation oscillator operating with 0.3 V-1.8 V unregulated supply. in *2018 IEEE Symposium on VLSI Circuits.* 119-120 (IEEE, 2018).

24 Hempel, M. *et al.* SynCells: A 60 x 60 μm^2 Electronic Platform with Remote Actuation for Sensing Applications in Constrained Environments. *ACS Nano* **15**, 8803-8812, (2021).

25 Masurkar, N., Babu, G., Porchelvan, S. & Arava, L. M. R. Millimeter-scale lithium ion battery packaging for high-temperature sensing applications. *J. Power Sources* **399**, 179-185, (2018).

26 Ferrari, S. *et al.* Latest advances in the manufacturing of 3D rechargeable lithium microbatteries. *J. Power Sources* **286**, 25-46, (2015).

27 Zheng, S. H., Shi, X. Y., Das, P., Wu, Z. S. & Bao, X. H. The road towards planar microbatteries and micro-supercapacitors: from 2D to 3D device geometries. *Adv. Mater.* **31**, 1900583, (2019).

28 Oudenhoven, J. F. M., Baggetto, L. & Notten, P. H. L. All-solid-state lithium-ion microbatteries: a review of various three-dimensional concepts. *Adv. Energy Mater.* **1**, 10-33, (2011).

29 Cao, D. X. *et al.* 3D printed high-performance lithium metal microbatteries enabled by nanocellulose. *Adv. Mater.* **31**, 1807313, (2019).

30 Shaijumon, M. M. *et al.* Nanoarchitectured 3D cathodes for Li-Ion microbatteries. *Adv. Mater.* **22**, 4978-4981, (2010).

31 Letiche, M. *et al.* Atomic layer deposition of functional layers for on chip 3D Li-ion all solid state microbattery. *Adv. Energy Mater.* **7**, 1601402, (2017).

32 Sun, P., Li, X., Shao, J. & Braun, P. V. High-performance packaged 3D lithium-ion microbatteries fabricated using imprint lithography. *Adv. Mater.* **33**, 2006229, (2021).

33 Wang, Y. X. *et al.* A reliable sealing method for microbatteries. *J. Power Sources* **341**, 443-447, (2017).

34 Su, Y. *et al.* LiPON thin films with high nitrogen content for application in lithium batteries and electrochromic devices prepared by RF magnetron sputtering. *Solid State Ionics* **282**, 63-69, (2015).

35 Le Cras, F., Pecquenard, B., Dubois, V., Phan, V. P. & Guy-Bouyssou, D. All-solid-state lithium-ion microbatteries using silicon nanofilm anodes: high performance and memory effect. *Adv. Energy Mater.* **5**, 1501061, (2015).

36 Lhermet, H. *et al.* Efficient power management circuit: from thermal energy harvesting to above-IC microbattery energy storage. *IEEE J. Solid-State Circuits* **43**, 246-255, (2008).

37 Oukassi, S. *et al.* Millimeter scale thin film batteries for integrated high energy density storage. in *2019 IEEE International Electron Devices Meeting (IEDM).* 26.21. 21-26.21. 24 (IEEE, 2019).

38 Fu, J. *et al.* Electrically rechargeable zinc-air batteries: progress, challenges, and perspectives. *Adv. Mater.* **29**, 1604685, (2017).

39 Li, Y. G. & Dai, H. J. Recent advances in zinc-air batteries. *Chem. Soc. Rev.* **43**, 5257-5275, (2014).

40 Zhang, J., Zhou, Q. X., Tang, Y. W., Zhang, L. & Li, Y. G. Zinc-air batteries: are they ready for prime time? *Chem. Sci.* **10**, 8924-8929, (2019).

41 Meskon, S., Othman, R. & Ani, M. A secondary, coplanar design Ni/MCM-41/Zn microbattery. in *IOP Conference Series: Materials Science and Engineering.* 012073 (IOP Publishing, 2018).

42 Liu, M. M. *et al.* Resist-dyed textile alkaline Zn microbatteries with significantly suppressed Zn dendrite growth. *ACS Appl. Mater. Inter.* **11**, 5095-5106, (2019).

43 Hao, Z. M. *et al.* On-Chip Ni-Zn microbattery based on hierarchical ordered porous Ni@$Ni(OH)_2$ microelectrode with ultrafast ion and electron transport kinetics. *Adv. Funct. Mater.* **29**, 1808470, (2019).

44 Chamran, F., Min, H. S., Dunn, B., Kim, C. J. & Ieee. Three-dimensional nickel-zinc microbatteries. in *2006 IEEE 19th International Conference on Micro Electro Mechanical Systems, Technical Digest.* 950-953 (IEEE, 2006).

45 Gerasopoulos, K., McCarthy, M., Royston, E., Culver, J. N. & Ghodssi, R. Nanostructured nickel electrodes using the Tobacco mosaic virus for microbattery applications. *J. Micromech. Microeng.* **18**, 104003, (2008).

46 Humble, P. H. & Harb, J. N. Optimization of nickel-zinc microbatteries for hybrid powered microsensor systems. *J. Electrochem. Soc.* **150**, A1182-A1187, (2003).

47 Singh, P., Wang, X. Q., LaFollette, R. & Reisner, D. RF-recharged microbattery for powering miniature sensors. in *Proceedings of the IEEE Sensors 2004.* (eds D. Rocha, P. M. Sarro, & M. J. Vellekoop) 349-352 (IEEE, 2004).

48 Wang, Y. *et al.* Wearable textile-based Co-Zn alkaline microbattery with high energy density and excellent reliability. *Small* **16**, 2000293, (2020).

49 Trocoli, R. *et al.* High specific power dual-metal-ion rechargeable microbatteries based on LiMn2O4 and zinc for miniaturized applications. *ACS Appl. Mater. Inter.* **9**, 32713-32719, (2017).

50 Zhu, M. S. *et al.* Light-permeable, photoluminescent microbatteries embedded in the color filter of a screen. *Energy Environ. Sci.* **11**, 2414-2422, (2018).

51 Ho, C. C., Evans, J. W. & Wright, P. K. Direct write dispenser printing of a zinc microbattery with an ionic liquid gel electrolyte. *J. Micromech. Microeng.* **20**, 104009, (2010).

52 He, B. *et al.* High-performance flexible all-solid-state aqueous rechargeable Zn-MnO2 microbatteries integrated with wearable pressure sensors. *J. Mater. Chem. A* **6**, 14594-14601, (2018).

53 Lai, W. H. *et al.* High performance, environmentally benign and integratable Zn//MnO_2 microbatteries. *J. Mater. Chem. A* **6**, 3933-3940, (2018).

54 Sun, G. Q., Jin, X. T., Yang, H. S., Gao, J. & Qu, L. T. An aqueous Zn-MnO_2 rechargeable microbattery dagger. *J. Mater. Chem. A* **6**, 10926-10931, (2018).

55 Wang, X. *et al.* Scalable fabrication of printed Zn//MnO_2 planar micro-batteries with high volumetric energy density and exceptional safety. *Natl. Sci. Rev.* **7**, 64-72, (2020).

56 Pique, A., Swider-Lyons, K. E., Weir, D. W., Love, C. T. & Modi, R. Laser direct writing of microbatteries for integrated power electronics. in *Laser Applications in Microelectronic and Optoelectronic Manufacturing VI.* (eds M. C. Gower, H. Helvajian, K. Sugioka, & J. J. Dubowski) 316-322 (2001).

57 Zhu, M. *et al.* A patternable and in situ formed polymeric zinc blanket for a reversible zinc anode in a skin‐mountable microbattery. *Adv. Mater.* **33**, 2007497, (2021).

58 Arnold, C. B., Kim, H. & Pique, A. Laser direct write of planar alkaline microbatteries. *Appl. Phys. A-Mater.* **79**, 417-420, (2004).

59 Ho, C. C., Murata, K., Steingart, D. A., Evans, J. W. & Wright, P. K. A super ink jet printed zinc-silver 3D microbattery. *J. Micromech. Microeng.* **19**, 094013, (2009).

60 Shi, J. J. *et al.* An ultrahigh energy density quasi-solid-state zinc ion microbattery with excellent flexibility and thermostability. *Adv. Energy Mater.* **9**, 1901957, (2019).

61 Bi, S. S., Wan, F., Huang, S., Wang, X. J. & Niu, Z. Q. A flexible quasi-solid-state bifunctional device with zinc-ion microbattery and photodetector. *Chemelectrochem* **6**, 3933-3939, (2019).

62 Li, R. *et al.* A flexible concentric circle structured zinc-ion micro-battery with electrodeposited electrodes. *Small Methods* **4**, 2000363, (2020).

63 Saputra, H., Othman, R., Ani, M. H., Sutjipto, A. G. E. & Muhida, R. High energy density zinc-air microbattery utilising inorganic MCM-41 membrane. *Mater. Res. Innov.* **15**, 114-117, (2011).

64 Synodis, M., Pikul, J., Allen, S. A. B. & Allen, M. G. Vertically integrated high voltage Zn-Air batteries enabled by stacked multilayer electrodeposition. *J. Power Sources* **449**, 227566, (2020).

65 Nadeau, P. *et al.* Prolonged energy harvesting for ingestible devices. *Nat. Biomed. Eng.* **1**, 0022, (2017).

66 Yin, L. *et al.* Materials, designs, and operational characteristics for fully biodegradable primary batteries. *Adv. Mater.* **26**, 3879-3884, (2014).

67 Chamran, F., Min, H. S., Dunn, B., Kim, C. & Ieee. Zinc-air microbattery with electrode array of zinc microposts. in *2007 IEEE 20th International Conference on Micro Electro Mechanical Systems*. 871-874 (IEEE, 2007).

68 Synodis, M., Pikul, J., Allen, S. A. B., Allen, M. & Ieee. Integrated fabrication of serially connected high voltage microbatteries via multilayer electrodeposition. in *2019 20th International Conference on Solid-State Sensors, Actuators and Microsystems & Eurosensors XXXIII*. 789-792 (IEEE, 2019).

69 Lee, K. B. & Lin, L. W. Electrolyte-based on-demand and disposable microbattery. *J. Microelectromech. Syst.* **12**, 840-847, (2003).

70 Armutlulu, A. *et al.* High-current zinc-air microbattery based on a micromachined multilayer lateral metallic scaffold. *Proc. of PowerMEMS*, 107-110, (2010).

71 Armutlulu, A. *et al.* A MEMS-enabled 3D zinc-air microbattery with improved discharge characteristics based on a multilayer metallic substructure. *J. Micromech. Microeng.* **21**, 104011, (2011).

72 Jimbo, H. & Miki, N. Gastric-fluid-utilizing micro battery for micro medical devices. *Sensor Actuat. B-Chem.* **134**, 219-224, (2008).

73 Zhang, H. *et al.* On-Chip Integration of a Covalent Organic Framework-Based Catalyst into a Miniaturized Zn–Air Battery with High Energy Density. *ACS Energy Letters* 10.1021/acsenergylett.1c00768, 2491-2498, (2021).

74 Bandodkar, A. J. *et al.* Sweat-activated biocompatible batteries for epidermal electronic and microfluidic systems. *Nat Electron* **3**, 554-+, (2020).

75 Shin, W., Lee, J., Kim, Y., Steinfink, H. & Heller, A. Ionic conduction in $Zn_3(PO4)_2$ $4H_2O$ enables efficient discharge of the zinc anode in serum. *J. Am. Chem. Soc.* **127**, 14590-14591, (2005).

76 Zheng, Y. F., Gu, X. N. & Witte, F. Biodegradable metals. *Materials Science and Engineering: R: Reports* **77**, 1-34, (2014).

77 Tsang, M., Armutlulu, A., Martinez, A. W., Allen, S. A. B. & Allen, M. G. Biodegradable magnesium/iron batteries with polycaprolactone encapsulation: A microfabricated power source for transient implantable devices. *Microsyst Nanoeng* **1**, (2015).

78 Souto, R. M., Gonzalez-Garcia, Y., Bastos, A. C. & Simoes, A. M. Investigating corrosion processes in the micrometric range: A SVET study of the galvanic corrosion of zinc coupled with iron. *Corros. Sci.* **49**, 4568-4580, (2007).

79 Li, J. *et al.* Surface evolution of a Pt-Pd-Au electrocatalyst for stable oxygen reduction. *Nat. Energy* **2**, 17111, (2017).

80 Tian, X. L. *et al.* Engineering bunched Pt-Ni alloy nanocages for efficient oxygen reduction in practical fuel cells. *Science* **366**, 850-856, (2019).

81 Cao, L. C., Fang, G., Cao, H. Z. & Duan, X. M. Photopatterning and electrochemical energy storage properties of an on-chip organic radical microbattery. *Langmuir* **35**, 16079-16086, (2019).

82 Hur, J. I., Smith, L. C. & Dunn, B. High areal energy density 3D lithium-ion microbatteries. *Joule* **2**, 1187-1201, (2018).
83 Liu, Q. W. *et al.* The first flexible dual-ion microbattery demonstrates superior capacity and ultrahigh energy density: small and powerful. *Adv. Funct. Mater.* **30**, 2002086, (2020).
84 Pikul, J. H., Liu, J. Y., Braun, P. V. & King, W. P. Integration of high capacity materials into interdigitated mesostructured electrodes for high energy and high power density primary microbatteries. *J. Power Sources* **315**, 308-315, (2016).
85 Yang, J. F. *et al.* Memristor Circuits for Colloidal Robotics: Temporal Access to Memory, Sensing, and Actuation. *Adv Intell Syst-Ger*, (2021).
86 Liu, Q. K. *et al.* Micrometer-sized electrically programmable shape-memory actuators for low-power microrobotics. *Sci Robot* **6**, eabe6663, (2021).
87 Molnar, A. C. *et al.* Nanoliter-Scale Autonomous Electronics: Advances, Challenges, and Opportunities. in *2021 IEEE Custom Integrated Circuits Conference (CICC)*. 1-6 (IEEE, 2021).

Acknowledgements

The authors are appreciative of funding from the US Army Research Office MURI grant on Formal Foundations of Algorithmic Matter and Emergent Computation (award no. W911NF-19-1-0233) for the metrological and computational tools utilized in this work. System fabrication and particulate engineering was supported using funds from the US Department of Energy (DOE), Office of Science, Basic Energy Sciences (grant DE-FG02-08ER46488). Microfabrication for this work was performed at the Harvard University Center for Nanoscale Systems (CNS), a member of the National Nanotechnology Coordinated Infrastructure Network (NNCI), which is supported by the National Science Foundation under NSF award no. 1541959. G. Z. acknowledges the support from MathWorks Engineering Fellowship. We acknowledge the help provided by Aubrey Penn at MIT.nano for providing help with collecting EDS data.

Author contributions

G.Z. conceived, designed, fabricated and characterized the picoliter batteries. D. G-M. and M. Z. M. provided the actuators. Y.Z. performed XRD measurement. V.B.K and J.Y. assisted with the cleanroom fabrication and writing. M.K. helped with STEM analysis, preparation of SWNT sensors and thermal evaporation. S.X.L. designed the sacrificial layer. A.T.L. assisted with characterization on probe station. J.Y. S.Y. and A.M.B. performed part of the actuator characterization. G.Z. and M.S.S. co-wrote the manuscript. All authors contributed to discussions.

Competing interests

The authors declare no competing interests.

Additional information

Correspondence and requests for materials should be addressed to M.S.S.